Deep learning assisted anode porous transport layer inverse design for proton exchange membrane water electrolysis

Xiaoxuan Yang [a], Mingliang Li [a], Jun Shen [b], Zhichun Liu [a], Wei Liu [a], Rui Long [a,*]

[a] *School of energy and power engineering, Huazhong University of Science and Technology, Wuhan 430074, PR China*
[b] *Hubei Research Center for New Energy & Intelligent Connected Vehicle, Wuhan University of Technology, Wuhan 430070, PR China*

ARTICLE INFO

ABSTRACT

Proton exchange membrane water electrolysis cell (PEMEC) offers a clean and promising way for hydrogen production. The spatial internal current density and temperature distribution uniformity significantly determines its reliability and durability, as well as the hydrogen production performance. Here, a non-isothermal 3D computational fluid dynamics (CFD) model for PEMEC with parallel flow fields is employed to investigate the impacts of the heterogeneous porosity distribution within the anode porous transport layer (APTL) on the internal current density and temperature distribution uniformity and energy conversion performance. 800 heterogeneous APTL porosity distributions are applied for CFD calculation, providing dataset for deep learning. The deep operator network (DeepONet) is employed to mapping the heterogeneous APTL porosity distribution to the real physical fields such as temperature, oxygen molar fraction and current density distribution fields. Full-connected neural network is employed to construct the relationship between the heterogeneous APTL porosity distribution to the performance metrics. The gradient descent algorithm is applied to obtain APTL porosity distributions corresponding to the optimal internal current density and temperature distribution uniformity, respectively. Compared with the uniform porosity distribution, the current density and temperature uniformity are improved by 45.544 % and 26.680 %, respectively, at an average APTL porosity of 0.5.

1. Introduction

Growing fossil fuel exploitation and consumption and the induced climate and environmental problems, as well as the imbalance between energy supply and demand have drawn increasing concern [1]. Hydrogen energy is considered a reliable alternative to traditional fossil fuels [2]. Among the developed hydrogen production ways, proton exchange membrane water electrolysis cell (PEMEC) has attracted attention for their faster response time, more compact structural design, higher current density and hydrogen purity [3,4].

Porous transport layer (PTL) plays a multitude of roles in PEMECs, including heat transfer, electrical conduction, oxygen and liquid water transport, and mechanical support [5-9]. Compared to the hydrogen precipitation reaction at the cathode, relatively slow oxygen precipitation reaction at the anode acts as the main limiting factor for the enhanced electrochemical performance of PEMEC [10]. Properties such as material, structural parameters and wettability of anode porous transport layer (APTL) have a significant impact on oxygen evolution reaction (OER), which in turn affects the overall performance of PEMEC

[11].

Numerical simulation is widely employed regarding the study on the PTL of the PEMEC, as experiments tend to have long time and high costs. Han et al. [12] developed a mathematical model to investigate the effect of contact angle, porosity and pore size of the diffusion layer on the performance and efficiency of PEMEC. They found that increasing the porosity and pore diameter and decreasing the contact angle can increase the saturation of liquid water along the thickness direction of the diffusion layer, thus improving the performance and efficiency of PEMEC. Zou et al. [13] showed that the increase of PTL thickness and porosity increases the ohmic overpotential. Toghyani et al. [14] developed a non-isothermal, fully 3D model for comprehensive analysis and discussed the effects of operating temperature, cathode pressure, film thickness, diffusion layer thickness and porosity on the electrolytic cell, revealing that thinner diffusion layers and larger porosities improve the performance. Liu et al. [15] investigated the effect of different PTL structures on oxygen transport, and found that higher porosity, larger fiber radius, and smaller anisotropy parameter are favorable for the formation of oxygen propagation paths.

The wettability of PTL and the interaction between PTL and catalyst

---

Abbreviation

ACL	anode catalyst layer
APTL	anode porous transport layer
BP	bipolar plate
CCL	cathode catalyst layer
CFD	computational fluid dynamics
CH	channel
CL	catalyst layer
CPTL	cathode porous transport layer
DeepONet	deep operator network
OER	oxygen evolution reaction
PEM	proton exchange membrane
PEMEC	proton exchange membrane water electrolysis cell
PTL	porous transport layer

Nomenclature

a_v	specific active surface areas (1/m)
C	substance concentration (mol/m^3)
C_p	specific heat capacity (J/(K kg))
D	pore size (m)
D_{ij}	diffusion coefficient (m^2/s)
E	electric energy consumed (kW h/m^3)
I	current (A)
$i0$	reference exchange current density (A/m^2)
iv	local electrochemical reaction rate (A/m^3)
j	current density (A/m^2)
K	permeability (m^2)
k	thermal conductivity (W/(K m))

p	pressure (Pa)
R	resistance (Ω)
R_{H2}	production rate of hydrogen (mol/s)
S	source term
T	temperature (K)
u	velocity (m/s)
U	Uniformity
V	voltage (V)
V_{eq}	hemodynamic equilibrium potential (V)
α	charge transfer coefficient
e	porosity
h	overpotential (V)
θ	covering coefficient
λ	water content
μ	dynamic viscosity (Pa/s)
ρ	density (kg/m^3)
σ	conductivity (S/m)
φ	potential (V)

Subscripts and superscripts

a	anode
act	activation
ave	average
c	cathode
eff	effective
fm	fluid
m	membrane
s	electronic
sa	solid

layer (CL) have also been considered. Li et al. [16] tuned the wettability of diffusion layers using a silane monolayer, and the experimental results showed that oxygen bubble separation was greater in diameter and frequency in the hydrophobic diffusion layer, which could lead to additional two-phase transport losses at current densities greater than 2 A/cm^2. Jiang et al. [17] investigated the wettability of PTL and CL by a 3D two-phase PEMEC model. They found that the combination of hydrophilic PTL and hydrophobic CL had better performance. Kang et al. [18] showed that the larger the porosity and smaller the pore size of the diffusion layer, the smaller the corresponding CL surface internal resistance and the higher the catalyst utilization. Wang et al. [19] fabricated a flow-enhanced liquid/gas diffusion layer using a wet etching method to facilitate material transfer in the area covered by the polar plate.

Schuler et al. [20] found that PTL with a layered structure increased catalyst utilization while reducing the mass transfer overpotential at the anode. It is furhter revealed by Lee et al. [21], who prepared PTLs with spatial gradients by vacuum plasma spraying. Employing a lower porosity near the CL and a higher porosity near the flow field resulted in a 29 % reduction in cell potential, a 38 % reduction in mass transfer overpotential, and a 50 % reduction in PTL gas saturation at a current density of 4.5 A/cm^2. Li et al. [22] developed a 2D two-phase flow model of PEMEC anode based on the VOF method to investigate the oxygen transport mechanism in PTL, revealing that there exists an ``isolation belt'' structure consisting of a series of narrow throats in the PTL, which prevents the merging of oxygen transport pathways. Zhou et al. [23] developed a 3D, isothermal, single-channel model that considered the porosity distribution along the flow direction, showing that increasing the porosity of APTL along the flow direction can improve the current density uniformity.

However, purely numerical calculations take up a large amount of computational resources, making it difficult to quickly obtain the physics fields and performance indexes under any given spatial

geometric or property distribution. In addition, the optimal spatial characteristic distributions could not be accurately achieved. Deep learning has been widely used in engineering design and prediction of multi-physics field systems, such as deep operator network (DeepONet) [24]. DeepONet, based on a general approximation theorem for operators, allows for efficient approximation of nonlinear operators in complex systems using relatively small datasets and provides real-time predictions for complex multi-physics field systems. Goswami et al. [25] proposed a physically based variational DeepONet for predicting crack paths in brittle materials and demonstrated its effectiveness through two benchmark tests of brittle fracture. Kumar et al. [26] applied DeepONet to accelerate the combustion chemistry of complex fuels. The method predicts the evolution of components and temperature over the relevant integration time and shows good prediction accuracy. Sahin et al. [27] implemented rib profile optimization for gas turbine internal cooling channels based on the DeepONet framework. Their proposed DeepONet uses stochastic continuous rib geometries with control points as inputs to output the pressure and heat transfer distributions around the shaped ribs. Shukla et al. [27] applied DeepONet to shape optimization of aircraft airfoils, where the model was able to predict the flow around arbitrary geometries with sufficiently excellent accuracy.

The inhomogeneous spatial current distribution and temperature distribution in the PEMEC degrade the reliability and durability, which are significantly impacted by heterogeneous APTL porosity distribution [28]. Previous studies regarding APTL porosity mainly involved APTLs with uniform porosity [12-15]. And the studies on inhomogeneous porosity are limited to the one-dimensional distribution along the flow direction [20-23]. Efforts regarding to spatial high-dimensional heterogeneous porosity distribution perpendicular to the APTL thickness direction has never been addressed. And the optimal spatial high-dimensional heterogeneous APTL porosity distributions leading to upgraded PEMEC performance have never been revealed. Here, a 3D non-isothermal CFD model of PEMEC with parallel flow fields is

employed to investigate the impacts of the heterogeneous spatial high-dimensional APTL porosity distribution on the internal current density and temperature distribution uniformity and energy conversion performance. 800 heterogeneous spatial high-dimensional APTL porosity distributions perpendicular to the APTL thickness direction are applied for CFD calculation, providing dataset for deep learning. The DeepONet is utilized for mapping the heterogeneous APTL porosity distribution to the real physical fields such as temperature, oxygen molar fraction and current density distribution fields. Neural network is employed to construct the relationship between the heterogeneous APTL porosity distribution to the performance metrics. The optimal APTL porosity distributions corresponding to the minimum internal current density and temperature distribution uniformity are further obtained via the gradient descent algorithm, respectively.

2. Material and methods

2.1. Physical model of the PEMEC

The structure and computational domain of the PEMEC is shown in Fig. 1. It consists of the proton exchange membrane (PEM), bipolar plates (BPs), channels (CHs), an anode/cathode porous transport layer (APTL/CPTL) and an anode/cathode catalyst layer (ACL/CCL). The materials of these components are also shown in Fig. 1. The material of BP and APTL is titanium; the material of CPTL is porous carbon; and the material of PEM is Nafion. The anode catalyst uses Ir, which has good catalytic activity and stability under acidic conditions, while the main component of the cathode catalyst is Pt.

The geometrical parameters of the model are listed in Table 1. Liquid water passes through the APTL to reach the ACL, where it is decomposed into protons, electrons and oxygen by the action of the catalyst and the external circuit.

$$H_2O \rightarrow 2H^+ + \frac{1}{2}O_2 + 2e^- \tag{1}$$

Protons pass through the PEM to the CCL, and react with electrons to produce hydrogen.

$$2H^+ + 2e^- \rightarrow H_2 \tag{2}$$
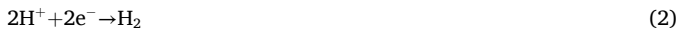
The numerical model consists of equations for the conservation of mass, momentum, charge and energy. In order to simplify the model, according to previous literatures [23,29,30]:, some assumptions were employed: (1) Single-phase flow was used to calculate the velocity and

Table 1
Geometric parameters of the PEMEC model.

Geometric parameter	Value
Reaction area	110 mm^2 (11 mm × 10 mm)
Inlet channel length	9.5 mm
Outlet channel length	9.5 mm
Parallel channel length	8 mm
Channel height	1 mm
Channel width	1 mm
BP thickness	1.5 mm
PTL thickness	0.3 mm
CL thickness	0.02 mm
PEM thickness	0.178 mm

pressure distributions of fluids; (2) The flow is assumed to be steady, incompressible and laminar; (3) Water is always in the liquid state and the process of phase change of water is neglected; (4) Water molecules pass through the proton exchange membrane under the action of electric tugging force is neglected, and the water content in the membrane was always saturated; (5) The gas cross-permeation effect is not taking into account.

2.1.1. Electrochemistry modeling

The electrochemical reactions at the anode and cathode in the PEMEC are given by the Butler–Volmer equation [31]:

$$i_{v,a} = a_{v,a} i_{0,a} (1 - \theta) \left(\exp\left(\frac{\alpha_a F \eta_{act}}{RT}\right) - \exp\left(-\frac{\alpha_c F \eta_{act}}{RT}\right) \right) \tag{3}$$

$$i_{v,c} = a_{v,c} i_{0,c} (1 - \theta) \left(\exp\left(\frac{\alpha_a F \eta_{act}}{RT}\right) - \exp\left(-\frac{\alpha_c F \eta_{act}}{RT}\right) \right) \tag{4}$$

where $i_{v,a}$ and $i_{v,c}$ are the local electrochemical reaction rates, $a_{v,a}$ and $a_{v,c}$ are the specific active surface areas, $i_{0,a}$ and $i_{0,c}$ are the reference exchange current densities, and α_a and α_c are the charge transfer coefficients. The subscripts a and c denote the anode and cathode respectively. Since the simulation involves higher current densities, the effect of bubbles covering the electrodes on the current density is considered in this paper, the covering coefficient θ is defined as $\theta = \left(\frac{j}{j_{lim}}\right)^{0.3}$, where j is the current density, $j_{lim} = 3 \times 10^5$ Am^{-2} is limiting current density [32]. η_{act} is the activation overpotential, which is the driving force for electron and ion transport.
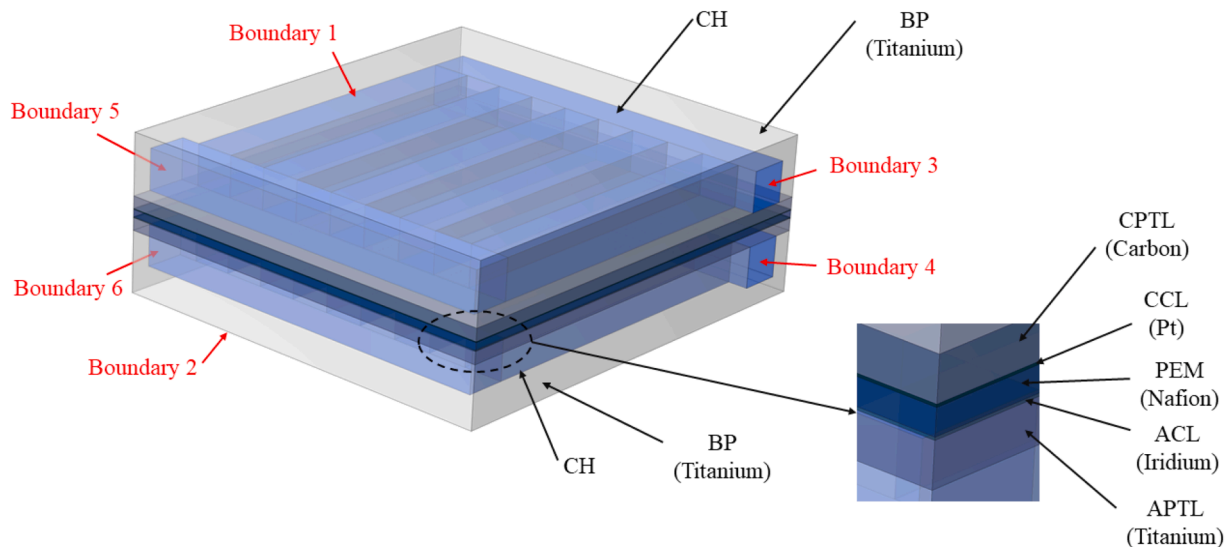
Fig. 1. Physical model and boundary distributions.

$$\eta_{act} = \varphi_s - \varphi_m - V_{eq} \tag{5}$$

where φ_m and φ_s are the electrolyte and solid phase potentials, respectively. V_{eq} is the thermodynamic equilibrium potential according to the Nernst equation, which neglects the influence of the component fraction. The potential at the cathode side is 0, so V_{eq} is the equilibrium potential of the anode and can be calculated by the following expression [33]:

$$V_{eq} = 1.229 - 9.0 \times 10^{-4}(T - 298.15) \tag{6}$$

The charge conservation equation for electrons and protons can be expressed as [34]:

$$\nabla \cdot \left(-\sigma_s^{eff} \nabla \varphi_s \right) = S_{\varphi,s} \tag{7}$$

$$\nabla \cdot (-\sigma_m \nabla \varphi_m) = S_{\varphi,m} \tag{8}$$

where $S_{\varphi,s}$, $S_{\varphi,m}$ are the current source terms at the anode and cathode respectively, σ_s^{eff} is the effective electronic conductivity, and σ_m is the electrolyte conductivity. The electrolyte conductivity is a function of water content and temperature [35]:

$$\sigma_m = (0.5139\lambda - 0.326)\exp\left(1268\left(\frac{1}{303} - \frac{1}{T}\right)\right) \tag{9}$$

where λ is the water content of the membrane, which in this paper is assumed to be saturated with a value of 14 [36]. Effective electronic conductivity is determined by the Bruggeman equation [23],

$$\sigma_m^{eff} = (1 - \varepsilon)^{1.5}\sigma_s \tag{10}$$

where ε is the porosity, σ_s is the conductivity of solid. Changes in porosity will have an effect on the contact resistance between the diffusion layer and the catalyst layer [21], which, according to the empirical equation, can be expressed as [18]

$$R = 0.014 \times \frac{d_0}{\varepsilon_0} \tag{11}$$

where d_0 and ε_0 are dimensionless coefficients, $d_0 = \frac{D}{1000}$, D is the pore size of the PTL, $\varepsilon_0 = \frac{\varepsilon}{0.1}$. Parameters used in electrochemistry modeling are shown in Table 2.

2.1.2. Mass transfer modeling

Continuity equation [41]:

$$\nabla \cdot (\varepsilon \rho \mathbf{u}) = 0 \tag{12}$$

where ρ is the density, and $\mathbf{u}$ is the mean velocity vector.

Momentum conservation equation [41]:

$$\nabla \cdot (\varepsilon \rho \mathbf{u}\mathbf{u}) = -\varepsilon \nabla p + \nabla \cdot (\varepsilon \mu \nabla \mathbf{u}) + S_u \tag{13}$$

where p is the pressure, μ is the dynamic viscosity, S_u is the momentum source term.

$$S_u = -\frac{\mu}{K}\varepsilon^2 \mathbf{u} \tag{14}$$

where K is the permeability. The permeability of the diffusion layer is determined by the Kozeny–Carman model [42]

$$K = \frac{D^2}{180}\frac{\varepsilon^3}{(1 - \varepsilon)^2} \tag{15}$$

The diffusion of gases is described by the component conservation equation [43]:

$$\nabla \cdot (\varepsilon \mathbf{u}_i C_i) = \nabla \cdot \left(D_{ij}^{eff} \nabla C_i \right) + S_i \tag{16}$$

where i, j is the different substance species (H_2O, O_2, H_2), C_i is the corresponding substance concentration, S_i is the source term of the corresponding substance, D_{ij}^{eff} is the effective diffusion coefficient of specie i and j, defined as follows [44]:

$$D_{ij}^{eff} = \varepsilon^{1.5}D_{ij}^0\left(\frac{T}{T_0}\right)^{1.5}\left(\frac{p_0}{p}\right) \tag{17}$$

2.1.3. Heat transfer modeling

The energy equation for heat transfer is described by Srinivasan [31]:

$$\nabla\left(\rho_{eff}C_{p,eff}\mathbf{u}T\right) = \nabla \cdot \left(k_{eff}T\right) + S_T \tag{18}$$

where S_T is the energy source term, ρ_{eff}, k_{eff} and $C_{p,eff}$ are the effective density, thermal conductivity and specific heat capacity, respectively.

$$\rho_{eff} = (1 - \varepsilon)\rho_{sa} + \varepsilon_x \rho_{fm} \tag{19}$$

$$C_{p,eff} = (1 - \varepsilon)C_{p,sa} + \varepsilon_x C_{p,fm} \tag{20}$$

$$k_{eff} = (1 - \varepsilon)k_{sa} + \varepsilon_x k_{fm} \tag{21}$$

where the subscripts sa and fm represent solid and fluid mixtures respectively.

The parameters used in the heat and mass transfer module are shown in Table 3. The source terms in the heat and mass transfer modeling are listed in Table 4.

2.1.4. Mesh independence check and model validation

The commercial software COMSOL Multiphysics was used to solve above governing equations. The boundaries of the model are presented in Fig. 1. In the calculation, liquid water enters the cell from boundaries 2 and 3 at a constant temperature $T_{in} = 40\,°C$ and flow rate $Q_{in} = 60$ mL/min. A constant pressure $p_0 = 1$ atm is applied at boundaries 5 and 6. A current density of 40,000 A/m² is applied at boundary 2, and Boundary 1 is grounded. The mesh independence check is performed at an

Table 2
Electrochemical parameters for the numerical calculation.

Parameter	Symbol	Value	Ref
Anode charge transfer coefficient	α_a	0.5	[37]
Cathode charge transfer coefficient	α_c	0.5	[37]
Anode reference exchange current density	$i_{0,a}$	0.1 A/m²	[38]
Cathode reference exchange current density	$i_{0,c}$	10000 A/m²	[38]
Anode specific reaction surface	$a_{v,a}$	1×10^5 1/m	[29]
Cathode specific reaction surface	$a_{v,c}$	1×10^6 1/m	[29]
Porosity of porous transport layer	ε_{CL}	0.25	[39]
Porosity of catalyst layer	ε_{PTL}	0.5	[40]
Faraday's constant	F	96,485 C/mol	
Universal gas constant	R	8.314 J/(mol K)	

Table 3
Parameters of the heat transfer modeling.

Parameter	Symbol	Value	Ref
Liquid water density	ρ_{H2O}	998 kg/m³	[45]
Membrane density	ρ_{mem}	1980 kg/m³	[46]
Ti density	ρ_{Ti}	4500 kg/m³	[47]
Specific heat capacities of membrane	$C_{p,mem}$	1090 J/(kg K)	[48]
Specific heat capacities of Ti	$C_{p,Ti}$	523 J/(kg K)	[47]
Specific heat capacities of H_2	$C_{p,H2}$	$28.89 – 8.314 \times 10^{-4}$ T + 1.914 × 10^{-6} T² J/(mol K)	[49]
Specific heat capacities of O_2	$C_{p,O2}$	$25.431 + 1.371 \times 10^{-2}$ T – 4.281 × 10^{-6} T² J/(mol K)	[49]
Thermal conductivity of membrane	k_{mem}	0.21 W/(m K)	[50]
Thermal conductivity of Ti	k_{Ti}	15.2 W/(m K)	[47]

Table 4

Source terms in the conservation equations.

Source terms	Units
$S_i = \begin{cases} -\|i_v\|M_{H_2O}/2F \\ \|i_v\|M_{O_2}/4F \\ \|i_v\|M_{H_2}/2F \end{cases}$	kg/(m³ s)
$S_u = -\dfrac{\mu}{K}\varepsilon^2 \mathbf{u}$	kg/(m² s)
$S_T = \begin{cases} \|i_v\|(\|\eta_{act,a}\|-(\Delta S_a T)/4F) + j^2/\sigma_s + j^2/\sigma_m \\ \|i_v\|(\|\eta_{act,c}\|-(\Delta S_c T)/4F) + j^2/\sigma_s + j^2/\sigma_m \\ j^2/\sigma_{BP} \\ j^2/\sigma_{PTL} \\ j^2/\sigma_{mem} \end{cases}$	W/m³
$S_{\varphi,s} = \begin{cases} i_v (\text{inanode}) \\ -i_v (\text{incathode}) \end{cases}$ $\quad S_{\varphi,m} = \begin{cases} -i_v (\text{inanode}) \\ i_v (\text{incathode}) \end{cases}$	A/m²

operating voltage of 2.0 V. Six mesh numbers are considered, including 53,721, 140,006, 265,591, 550,826, 1,026,052, and 1,802,809. As shown in Fig. 2, the relative errors of the current density and the average temperature of the ACL at mesh numbers 1,023,052 and 1,802,809 are 0.015 % and 0.001 %, respectively. In order to reasonably allocate computational resources, the mesh number of 1,026,052 is employed in the following calculations.

To ensure the accuracy of the model, the polarization curve calculated at $Q_{in} = 15$ mL/s, $T_{in} = 45$ °C were compared with the experimental data from Majasan et al. [51]. As shown in Fig. 3, the simulation results are in good agreement with the experimental data, which justifies the model employed in present study.

2.2. Deep learning

Fig. 4 shows a schematic of the architecture of DeepONet, which consists of a trunk network and a branch network. p is the width of the network. The network takes inputs composed of two parts: u and y, and outputs $G(u)(y)$. The trunk network is responsible for processing the domain of the input function, which takes y as input and outputs a set of feature vectors corresponding to the points on the input domain $[t_1, t_2, ..., t_p]^T \in R^P$. The branch network is responsible for processing the input function which takes $[u(x_1), u(x_2), ..., u(x_m)]^T$ as inputs, and outputs a scalar $b_k \in R$ for $k = 1,2,...,p$. For data generation, we use the mean-zero Gaussian random fields for the input function $u(x)$:

$$u(x) \sim GP(0, k_l(x_1, x_2)) \tag{22}$$

where the covariance kernel $k_l(x_1, x_2) = \exp\left(-\|x_1 - x_2\|^2 /2l^2\right)$ is the Gaussian kernel with a length scale parameter $l > 0$. The length-scale l determines the smoothness of the sampled function, and larger l leads to smoother u [24].
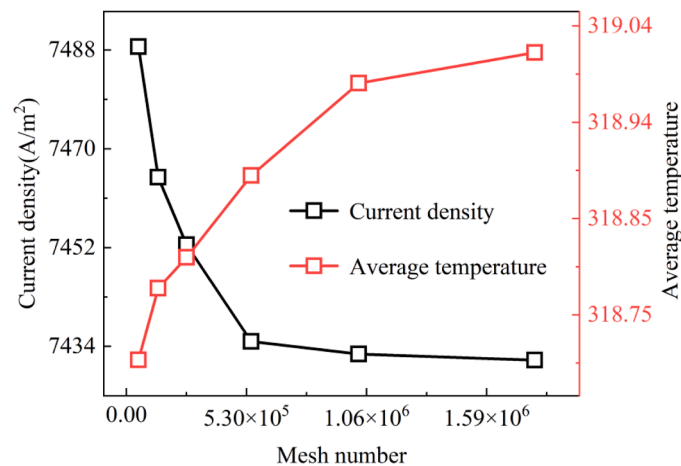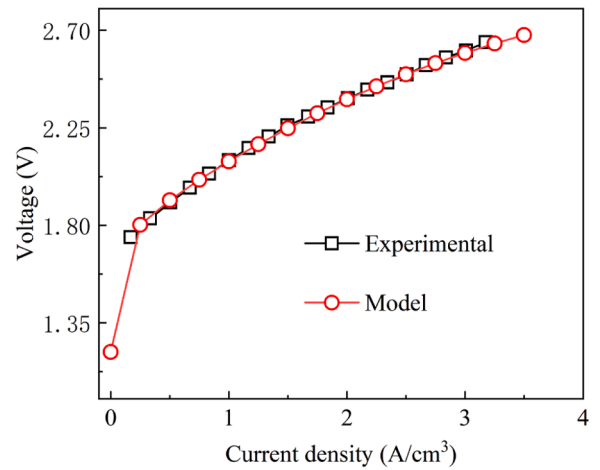
Fig. 2. Mesh independence check.

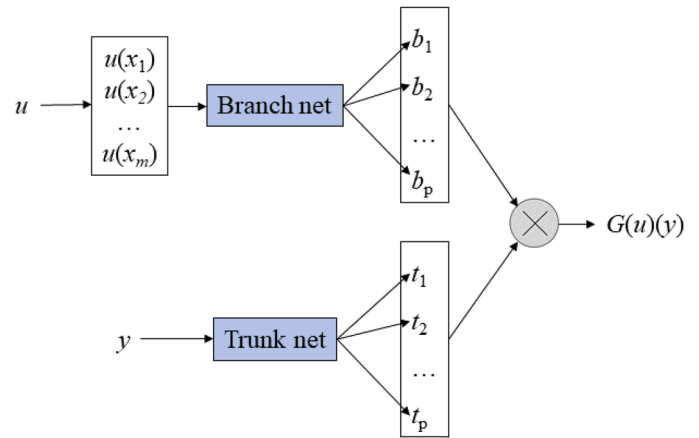**Fig. 3.** Comparison of polarization curves.

Fig. 4. The DeepONet architecture.

The output of the branch network is dot-produced or otherwise combined with the output of the backbone network to generate a prediction of the response of the input function at a particular domain point, and the output can be expressed as [24]:

$$G(u)(y) \approx \sum_{k=1}^{p} \underbrace{b_{..}(u(x_1), u(x_2), ..., u(x_m))}_{\text{branch}} \underbrace{t_{..}(y)}_{\text{trunk}} \tag{23}$$

The loss function applied here is the relative root-mean-square errors (r.m.s.e.) between the true value of $G(u)(y)$ and the network prediction for the input ($[u(x_1), u(x_2), ..., u(x_m)]$, y). In this work, the DeepONet is utilized for mapping the heterogeneous APTL porosity distribution to the real physical fields such as temperature, oxygen molar fraction and current density distribution fields. The prediction of performance metrics is conducted via full-connected neural networks with the APTL porosity distribution as the input.

3. Results and discussion

3.1. Effects of spatial heterogeneous APTL porosity distribution

In order to investigate the effect of the heterogeneous APTL porosity on the performance of the cell, different heterogeneous porosity distributions were randomly generated for calculation. Three random porosity distributions with an average porosity of 0.5 were selected and named R1, R2, R3. The performance under the uniform porosity is also calculated and compared. Since this study focus on the APTL porosity,

the physical fields presented are selected from the anode side. The temperature field and oxygen molar fraction field are located at the interface between the flow field and the APTL, and the current density field is chosen at the interface between the ACL and the PEM.

Fig. 5 shows the temperature, oxygen mole fraction and current density distributions for four different porosity distributions under the average porosity of 0.5. Among them, ``Uniform'' is the uniform porosity distribution, while R1, R2 and R3 are three different random porosity distributions. As shown in Fig. 5, for the uniform porosity configuration, higher values of temperature and current density occur in the upper left corner. Non-uniform temperature and current density distribution present a negative impact on the stability and lifetime of the PEMEC. It is worth mentioning that the temperature presents a higher value at the corresponding location of the flow channel, due to the fact that the heat transfer coefficient of the metallic material is higher than that of the fluid. The temperature and current density distribution vary obviously under different porosity distributions. The locations of oxygen aggregation in the APTL also exhibit different behaviors. R1 configuration leads to more uniform temperature and current density distribution than the electrolytic cell with uniform porosity.

To better evaluate the uniformity of the temperature distribution and current density distribution, the uniformity indices U_φ is defined as follows [52]:

$$U_{-}\varphi = \frac{\int_A |\varphi - \varphi_{avg}| dA}{\int_A \varphi_{avg} dA} \qquad (24)$$

where φ and φ_{avg} are the local and average values of the interfaces,

respectively. The energy consumption of the cell is given by Wei et al. [29]:

$$E = \frac{V_{cell} \cdot I_{cell}}{R_{H_2} \cdot 3600 \cdot 22.4} \qquad (25)$$

where E is the electric energy consumed to produce hydrogen per unit volume in the standard state, V_{cell} and I_{cell} are the voltage and current of the cell, respectively. R_{H2} is the production rate of hydrogen,

$$R_{H_2} = \frac{\nu_{H_2} i_v}{nF} \qquad (26)$$

where the ν_{H2} is the stoichiometric number of hydrogen, and n is the number of electrons involved in the reaction.

Fig. 6 is the comparison of the performances depending on porosity distributions. The voltage, energy consumption, temperature uniformity index U_T at the APTL-flow field interface and current density uniformity index U_I at the ACL-PEM interface were compared. As shown in Fig. 6(a) and (b), for electrolytic cells with different porosity distributions, their voltage and energy consumption do not change obviously. It suggests that the porosity distribution has a limited effect on the voltage and energy consumption of the electrolytic cell. However, as seen in Fig. 6(c) and (d), there is a big difference of the uniformity indices of current density and temperature under different APTL porosity distributions. The current density uniformity index U_I under R1 distribution is 0.01834, which is 22.1 % lower than that under the uniform porosity configuration. The temperature uniformity index U_T for the R1 distribution is 0.00845, which is 17.4 % lower than that under the uniform porosity configuration. It indicates that the APTL porosity distribution
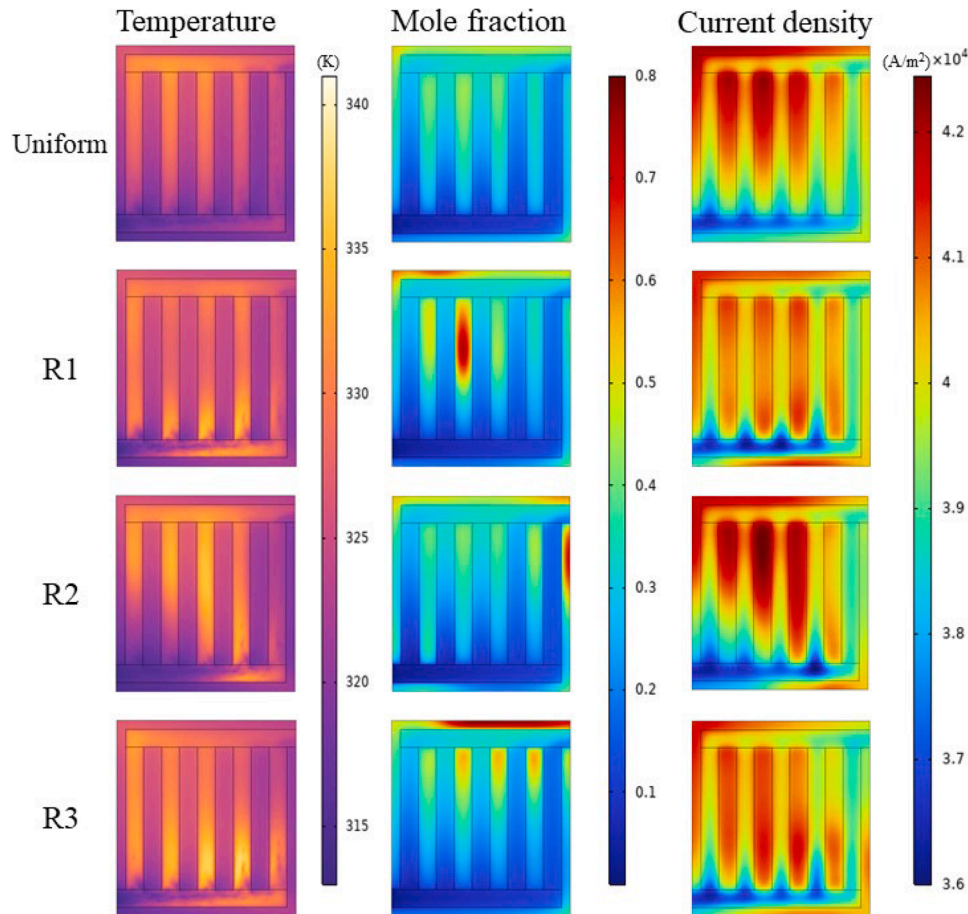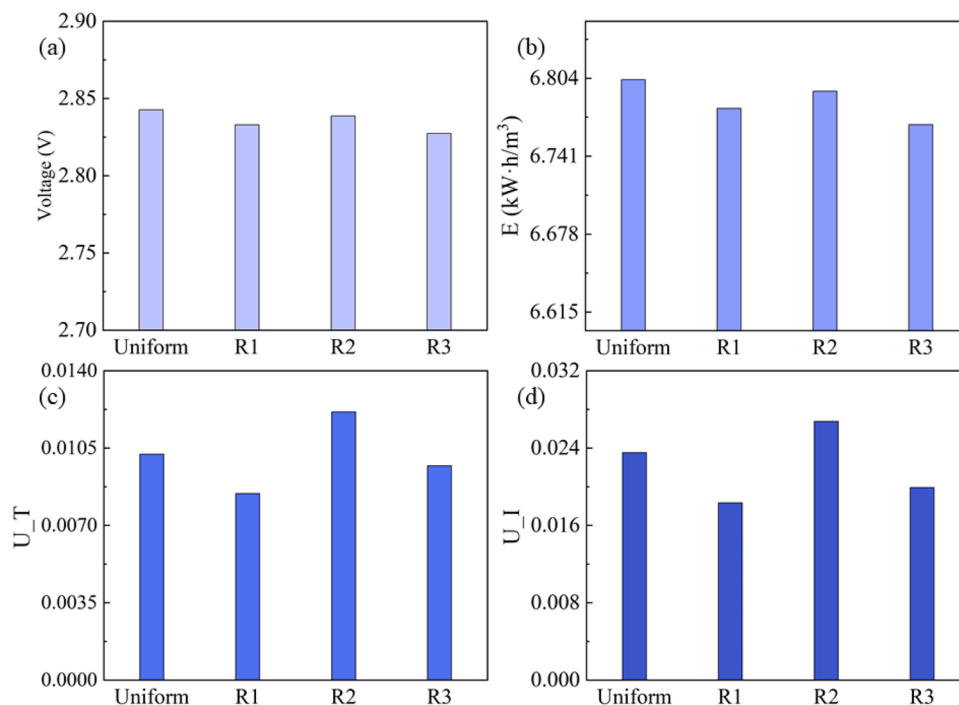

Fig. 5. Temperature, oxygen mole fraction, and current density distributions under an average APTL porosity of 0.5. 'Uniform' is a uniformly distributed porosity, and R1, R2, and R3 are three random porosity distributions.

Fig. 6. Comparison of the performances depending on porosity distributions; (a) voltage, (b) energy consumption, (c) temperature uniformity index U_T at the APTL-flow field interface, (d) current density uniformity index U_I at the ACL-PEM interface.

has a significant effect on the uniformity indices. It is highly demanded to optimize the APTL porosity distribution for better uniformity indices.

3.2. Deep learning assisted physical field and performance metrics prediction

800 sets of random porosity distributions were generated, of which 700 sets were used for training the system and the remaining 100 sets were used for testing the system. A set of test results from the test set is presented here. Fig. 7 shows the chosen test porosity distribution. The tested and predicted current density, temperature, and oxygen mole fraction fields are compared in Fig. 8, where the test data are from the CFD calculation and the prediction data are generated from the Deep-ONet. As shown in Fig. 8, the predicted physical fields agree well with
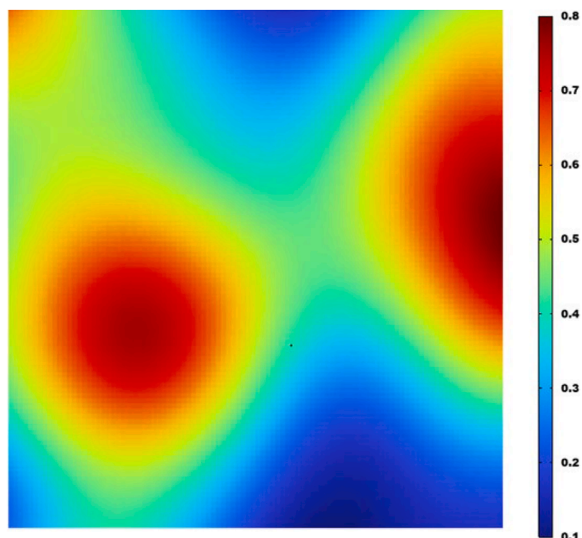
Fig. 7. Randomly generated porosity distribution.

the CFD calculated ones. The r.m.s.e. between the predicted and CFD calculated values of the three physical quantity fields are 0.18 %, 1.31 %, and 0.05 %, respectively. Therefore, the DeepONet is able to accurately predict the distribution of current density, temperature and oxygen mole fraction in the electrolytic cell.

Fig. 9 shows the relative r.m.s.e. of the energy consumption, voltage obtained via the full-connected neural network, and temperature uniformity index and current density uniformity index calculated via the physical field generated by the DeepONet. The blue dots represent outliers. The box plot covers the interval from the 25th percentile to the 75th percentile, with the mean (50th percentile) shown as a red line. The blue lines represent mean values. The relative r.m.s.e. for all physical quantities are less than 5 %. The employed deep learning models can accurately predict the physical quantities.

3.3. Heterogeneous APTL porosity optimization for current density uniformity

Fig. 10 shows the optimized APTL porosity distribution under the objective of minimum current density uniformity index. Under an average porosity of 0.5, the current density distribution of the optimized cell is more uniform compared to that under the uniform porosity configuration. The area with higher current density in the upper left corner is greatly attenuated. It can also be noticed that the temperature distribution of the electrolytic cell has also been improved considerably. The voltage, energy consumption, temperature uniformity index and current density uniformity index of the optimized electrolytic cell are 2.827 V, 6.768 kW h/m^3, 0.00749, and 0.0128, respectively. Compared to that under the uniform porosity configuration, reductions of 26.680 %, and 45.544 % in temperature uniformity index and current density uniformity index are achieved, respectively.

At an average porosity of 0.3, oxygen accumulates under the bipolar plates of the cell, resulting in a higher molar fraction of oxygen in the diffusion layer. However, due to the better thermal conductivity of the diffusion layer at lower porosity, the corresponding temperature distribution is more uniform. At an average porosity of 0.7, the local temperature and current density of the electrolytic cell increase
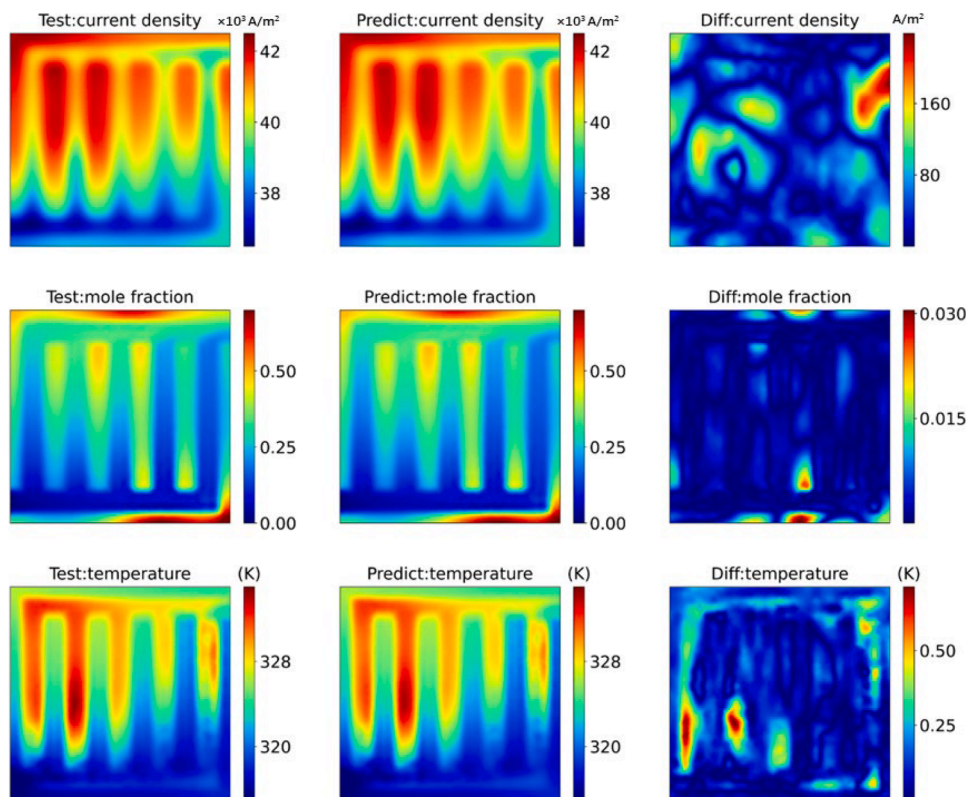
Fig. 8. Comparison of the predicted and the CFD calculated physical fields.
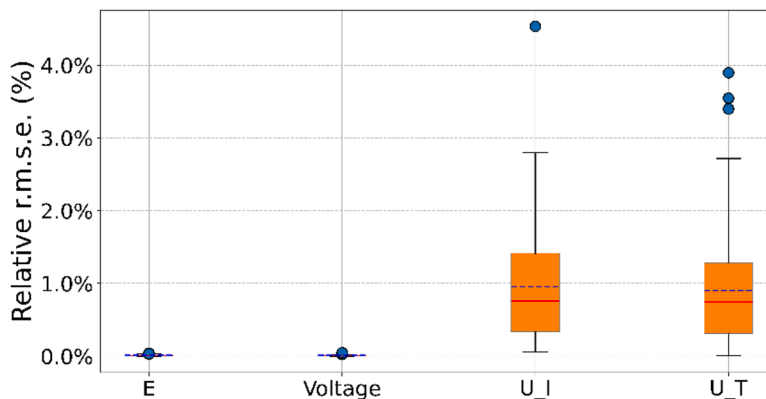

Fig. 9. Relative r.m.s.e. of the energy consumption, voltage obtained via the full-connected neural network, and temperature uniformity index and current density uniformity index obtained via the DeepONet.

dramatically, while the oxygen mole fraction in the diffusion layer is low and uniformly distributed. This is due to the fact that the larger porosity facilitates the timely discharge of oxygen and promotes the electrochemical reaction. Although the optimal APTL porosity distribution is irregular, the porosity near the inlet side is larger while the porosity in the upper left corner is smaller.

As depicted in Fig. 11, the voltage and energy consumption under the optimal conditions decreases with increasing average APTL porosity. The optimized temperature uniformity index increases with increasing average porosity. However, it is worth mentioning that the optimal current density uniformity of the electrolytic cell presents the smallest value at an average porosity is 0.5. An increase in porosity facilitates the diffusion of oxygen. However, it leads to a decrease in the conductivity of the diffusion layer. The former promoting electrochemical reactions while the latter inhibiting electron transfer. The comprise between these two effects accounts for this phenomenon.

3.4. Heterogeneous APTL porosity optimization for temperature uniformity

Figs. 12 and 13 show the optimal results with the temperature uniformity index as the optimization objective. The optimized voltage, energy consumption, temperature uniformity index and current density uniformity index are 2.835, 6.784, 0.00744, 0.0174, respectively, at an average porosity of 0.5. Compared to that under the uniform porosity configuration, reductions of 0.268 %, 0.278 %, 27.239 %, and 26.066 %, respectively are presented in voltage, energy consumption, temperature uniformity index and current density uniformity index. With temperature uniformity improved, current density uniformity was sacrificed. Compared to the results under the optimization for current density
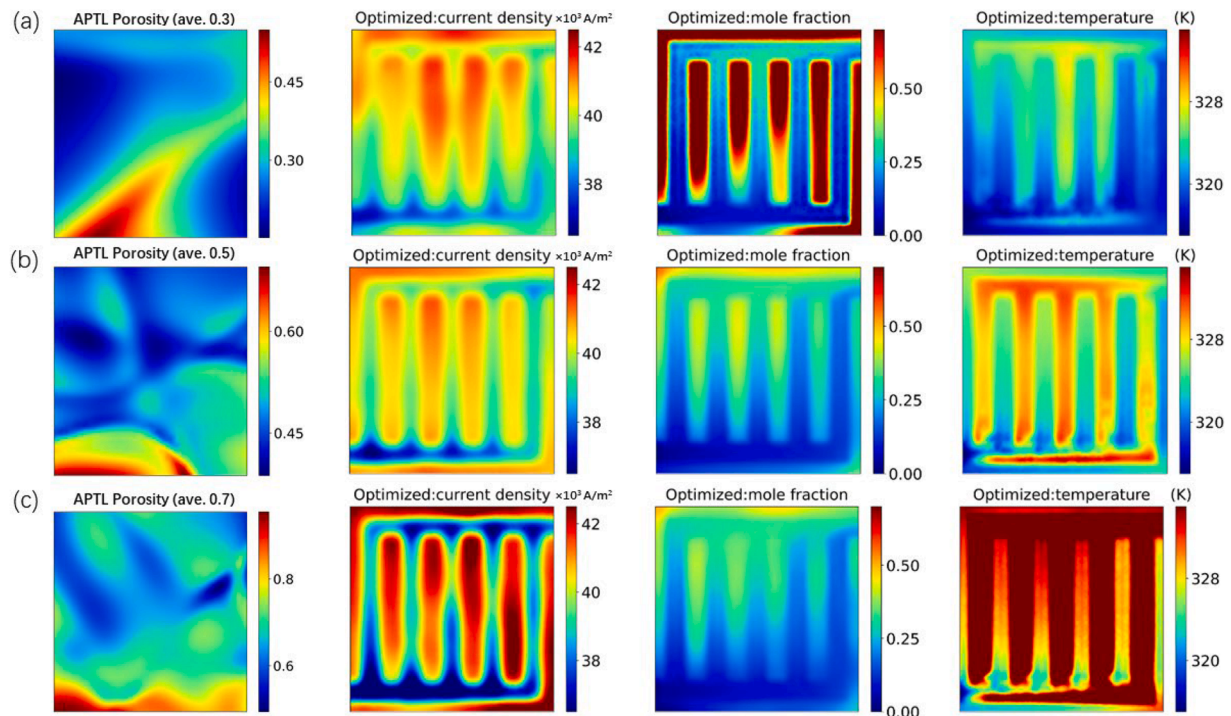
Fig. 10. Optimal porosity distribution and corresponding current density, oxygen mole fraction, and temperature distributions for different average APTL porosities for minimizing current density uniformity index.
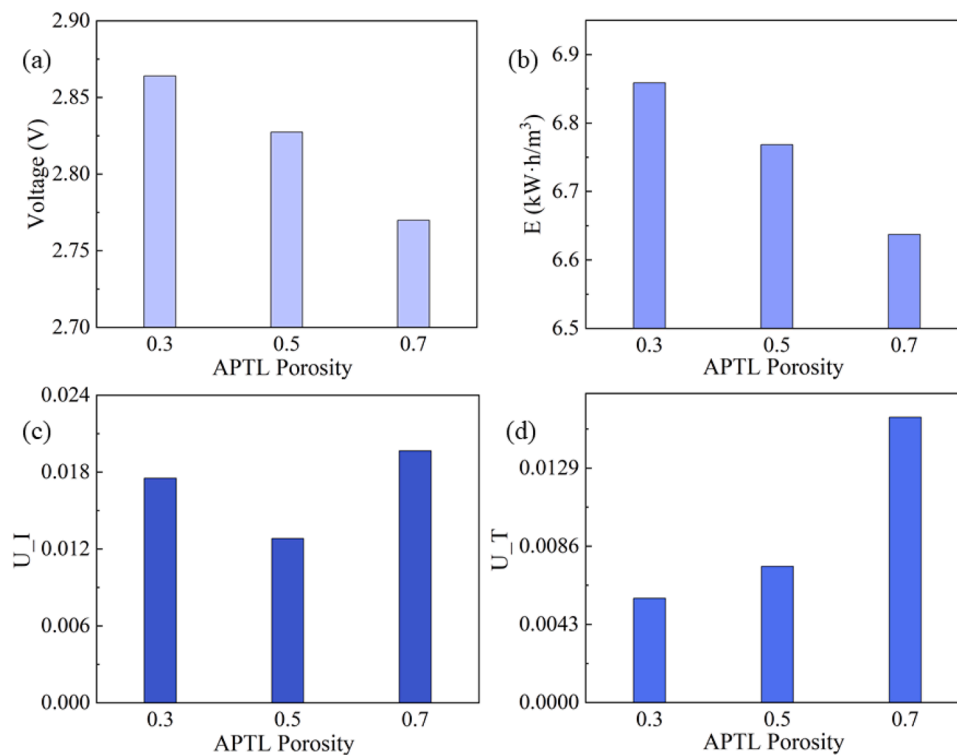

Fig. 11. Comparison of the performances depending on different average APTL porosities for minimizing current density uniformity index; (a) voltage, (b) energy consumption E, (c) temperature uniformity index U_T at the APTL-flow field interface, (d) current density uniformity index U_I at the ACL-PEM interface.

uniformity, the temperature uniformity improves by 0.696 % when the temperature uniformity index is optimized, meanwhile the corresponding current density uniformity is decreased by 35.780 %.

As shown in Figs. 10 and 12, it can be found that the optimal APTL porosity distribution corresponding to the minimal temperature

uniformity is more irregular. It roughly conforms to the distribution pattern of larger porosity near the entrance and smaller porosity in the upper left corner. At an average porosity of 0.3, the cells have higher local current density and temperature, leading to worsen uniformity, due to the fact that a larger porosity corresponds to a smaller thermal
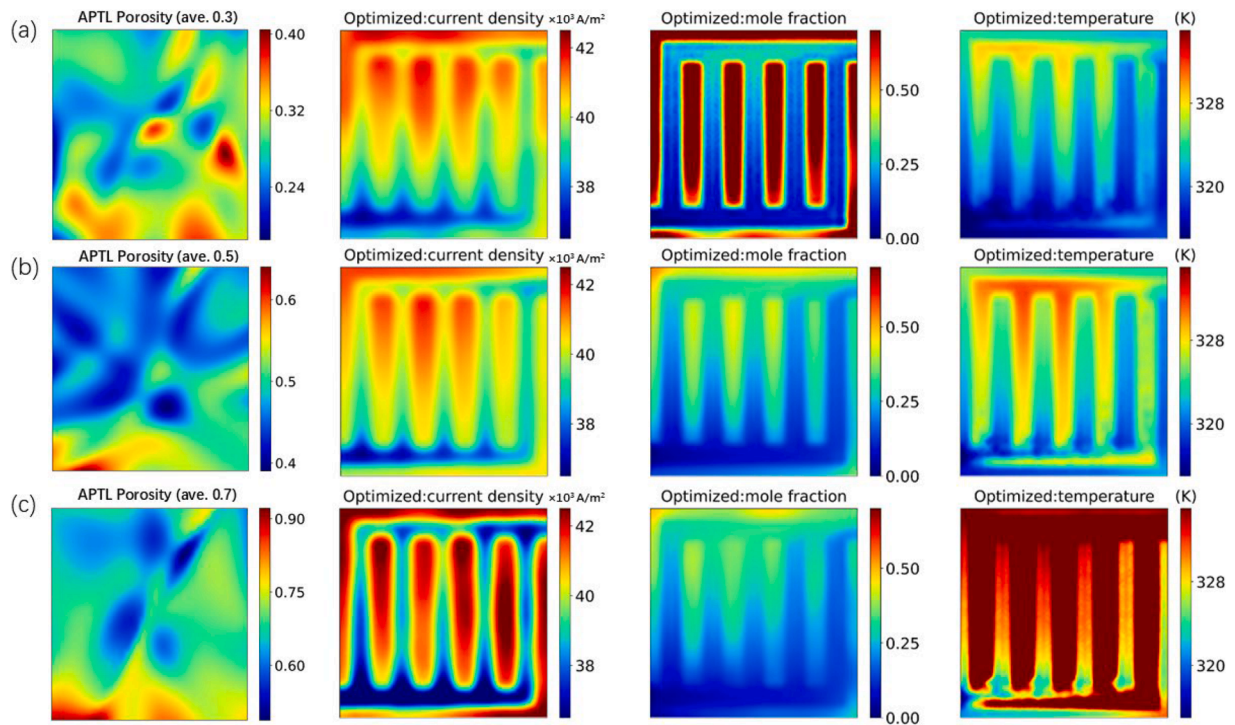
Fig. 12. Optimal porosity distribution and corresponding current density, oxygen mole fraction, and temperature distributions for different average APTL porosities for minimizing temperature uniformity.
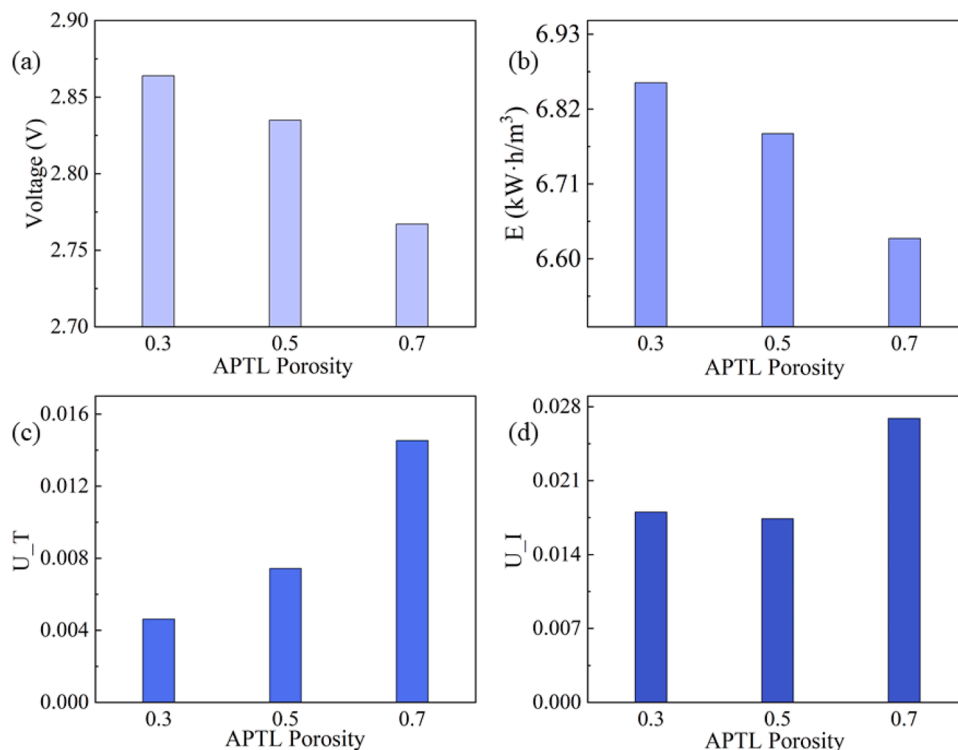

Fig. 13. Comparison of the performances depending on different average APTL porosities for minimizing temperature uniformity; (a) Voltage, (b) energy consumption E, (c) temperature uniformity index U_T at the APTL-flow field interface, (d) current density uniformity index U_I at the ACL-PEM interface.

conductivity and electrical conductivity, which weakens the heat transfer capacity and generates more Joule heat. The current density distributions under average APTL porosities of 0.5 and 0.3 exhibit similar trend, while the temperature distributions and oxygen mole fraction distributions are more disparate. This is due to the fact that smaller porosity has better thermal and electrical conductivity, while larger porosity is more favorable for oxygen diffusion. The compromised impacts account for this phenomenon. Unlike optimizing current density uniformity, when temperature uniformity is the optimization objective, a smaller APTL porosity is more appealing.

4. Conclusions

In present study, a 3D non-isothermal model of PEMEC with parallel flow fields is employed to investigate the impacts of the heterogeneous APTL porosity distribution on the spatial internal current density and temperature distribution uniformity and energy conversion performance of the PEMEC. The APTL porosity has a limited effect on the voltage and energy consumption of the PEMEC. However, it can significantly impact the temperature and current density uniformity. The employed deep learning models can accurately predict the distribution of current density, temperature and oxygen mole fraction fields and the performance metrics. In addition, the optimal APTL porosity distributions corresponding to the minimum internal current density and temperature distribution uniformity have been achieved, respectively. In the optimal porosity distributions for minimum current density and temperature distribution uniformity, the porosity near the inlet side is large, while the porosity in the upper left corner is small. A smaller average porosity leads to a lower temperature uniformity index, while a larger average porosity renders lower energy consumption and better mass transfer performance. Compared with the uniform porosity distribution, the current density and temperature uniformity are improved by 45.544 % and 26.680 %, respectively, at an average APTL porosity of 0.5.

Present work provides an efficient way to obtain the desired spatial heterogeneous APTL porosity distribution. The results can serve as a guide for future experimental studies. Although the analysis is conducted on PEMECs with parallel flow fields, the proposed method is versatile and can be extended to cells featuring different flow field structures, geometries, materials, and diverse operational conditions. However, the present study is based on numerical simulations, including CFD tests and DeepONet predictions, without corresponding experimental validation. Future research should address this gap by prioritizing the experimental verification of the optimized porosity distributions to enhance the validity and practical applicability. Additionally, the development of a cost-effective method for precise regulation of porosity distribution is also challenging, which should be addressed for the practical implementation of APTLs with spatial heterogeneous porosities in engineering applications.

CRediT authorship contribution statement

Xiaoxuan Yang: Writing – original draft, Visualization. **Mingliang Li:** Methodology. **Jun Shen:** Visualization. **Zhichun Liu:** Funding acquisition. **Wei Liu:** Formal analysis. **Rui Long:** Writing – review & editing, Conceptualization.

Declaration of competing interest

The authors declare that they have no known competing financial interests or personal relationships that could have appeared to influence the work reported in this paper.

Data availability

Data will be made available on request.

Acknowledgments

References

[1] G. Hu, C. Chen, H.T. Lu, Y. Wu, C. Liu, L. Tao, Y. Men, G. He, K.G. Li, A review of technical advances, barriers, and solutions in the power to hydrogen (P2H) roadmap, Engineering 6 (2020) 1364–1380.

[2] Y. Elaouzy, A. El Fadar, Water-energy-carbon-cost nexus in hydrogen production, storage, transportation and utilization, Int. J. Hydrogen Energy 53 (2024) 1190–1209.

[3] A.H. Abdol Rahim, A.S. Tijani, S.K. Kamarudin, S. Hanapi, An overview of polymer electrolyte membrane electrolyzer for hydrogen production: modeling and mass transport, J. Power Sources 309 (2016) 56–65.

[4] J. Valentín-Reyes, M.I. León, T. Pérez, T. Romero-Castañón, J. Beltrán, J.R. Flores-Hernández, J.L. Nava, Simulation of an interdigitated flow channel assembled in a proton exchange membrane fuel cell (PEMFC), Int. J. Heat Mass Transf. 194 (2022) 123026.

[5] C. Romero, D. Benedetto, E. Gordo, Processing and surface modification of titanium open cell porous structures for PEM fuel cell bipolar plates, Int. J. Hydrogen Energy 52 (2024) 1190–1201.

[6] O. Panchenko, E. Borgardt, W. Zwaygardt, F.J. Hackemüller, M. Bram, N. Kardjilov, T. Arlt, I. Manke, M. Müller, D. Stolten, W. Lehnert, In-situ two-phase flow investigation of different porous transport layer for a polymer electrolyte membrane (PEM) electrolyzer with neutron spectroscopy, J. Power Sources 390 (2018) 108–115.

[7] H. Ito, T. Maeda, A. Nakano, C.M. Hwang, M. Ishida, A. Kato, T. Yoshida, Experimental study on porous current collectors of PEM electrolyzers, Int. J. Hydrogen Energy 37 (2012) 7418–7428.

[8] M. Suermann, K. Takanohashi, A. Lamibrac, T.J. Schmidt, F.N. Büchi, Influence of operating conditions and material properties on the mass transport losses of polymer electrolyte water electrolysis, J. Electrochem. Soc. 164 (2017) F973–F980.

[9] C. Liu, Noble Metal Coated Porous Transport Layers for Polymer Electrolyte Membrane Water Electrolysis, (2021).

[10] Y. Wang, Y. Pang, H. Xu, A. Martinez, K.S. Chen, PEM Fuel cell and electrolysis cell technologies and hydrogen infrastructure development—A review, Energy Environ. Sci. 15 (2022) 2288–2328.

[11] L. Jianxin, L. Zongqi, Z. Xiaolei, H. Gulizhaina, C. Xuedi, Wettability and wettability modification methods of porous transport layer in polymer electrolyte membrane electrolysis cells (PEMEC): a review, Int. J. Hydrogen Energy 48 (2023) 26629–26651.

[12] B. Han, J. Mo, Z. Kang, F.-Y. Zhang, Effects of membrane electrode assembly properties on two-phase transport and performance in proton exchange membrane electrolyzer cells, Electrochim. Acta 188 (2016) 317–326.

[13] L. Zou, Q. Shen, J. Liao, L. Xu, G. Yang, S. Li, Effect of porous transport layer parameters on the proton exchange membrane electrolyzer performance, Chem. Phys. Lett. 823 (2023) 140570.

[14] S. Toghyani, E. Afshari, E. Baniasadi, S.A. Atyabi, G.F. Naterer, Thermal and electrochemical performance assessment of a high temperature PEM electrolyzer, Energy 152 (2018) 237–246.

[15] J. Liu, M. Li, Y. Yang, N. Schlüter, D. Mimic, D. Schröder, Tailored porous transport layers for optimal oxygen transport in water electrolyzers: combined stochastic reconstruction and lattice Boltzmann method, Chem. Phys. Chem. 24 (2023) e202300197.

[16] Y. Li, Z. Kang, X. Deng, G. Yang, S. Yu, J. Mo, D.A. Talley, G.K. Jennings, F.-Y. Zhang, Wettability effects of thin titanium liquid/gas diffusion layers in proton exchange membrane electrolyzer cells, Electrochim. Acta 298 (2019) 704–708.

[17] Y. Jiang, Y. Li, Y. Ding, S. Hu, J. Dang, F. Yang, M. Ouyang, Simulation and experiment study on two-phase flow characteristics of proton exchange membrane electrolysis cell, J. Power Sources 553 (2023) 232303.

[18] Z. Kang, J. Mo, G. Yang, Y. Li, D.A. Talley, B. Han, F.-Y. Zhang, Performance modeling and current mapping of proton exchange membrane electrolyzer cells with novel thin/tunable liquid/gas diffusion layers, Electrochim. Acta 255 (2017) 405–416.

[19] W. Wang, L. Ding, Z. Xie, S. Yu, C.B. Capuano, A. Keane, K. Ayers, F.Y. Zhang, 3D structured liquid/gas diffusion layers with flow enhanced microchannels for proton exchange membrane electrolyzers, Energy Convers. Manag. 296 (2023) 117665.

[20] T. Schuler, J.M. Ciccone, B. Krentscher, F. Marone, C. Peter, T.J. Schmidt, F. N. Büchi, Hierarchically structured porous transport layers for polymer electrolyte water electrolysis, Adv. Energy Mater. 10 (2019) 1903216.

[21] J.K. Lee, C. Lee, K.F. Fahy, P.J. Kim, J.M. LaManna, E. Baltic, D.L. Jacobson, D. S. Hussey, S. Stiber, A.S. Gago, K.A. Friedrich, A. Bazylak, Spatially graded porous transport layers for gas evolving electrochemical energy conversion: high performance polymer electrolyte membrane electrolyzers, Energy Convers. Manage. 226 (2020) 113545.

[22] Q. Li, C. Bao, Z. Jiang, X. Zhang, T. Ding, C. Fang, M. Ouyang, Numerical study on oxygen transport pattern in porous transport layer of proton exchange membrane electrolysis cells, eTransportation 15 (2023) 100210.

[23] H. Zhou, B. Chen, K. Meng, M. Luo, P. Li, Z. Tu, Combination effect of flow channel configuration and anode GDL porosity on mass transfer and performance of PEM water electrolyzers, Sustain. Energy Fuels 6 (2022) 3944–3960.

[24] L. Lu, P. Jin, G. Pang, Z. Zhang, G.E. Karniadakis, Learning nonlinear operators via DeepONet based on the universal approximation theorem of operators, Nat. Mach. Intell. 3 (2021) 218–229.

[25] S. Goswami, M. Yin, Y. Yu, G.E. Karniadakis, A physics-informed variational DeepONet for predicting crack path in quasi-brittle materials, Comput. Methods Appl. Mech. Eng. 391 (2022) 114587.

[26] A. Kumar, T. Echekki, Combustion chemistry acceleration with DeepONets, Fuel 365 (2024) 131212.

[27] I. Sahin, C. Moya, A. Mollaali, G. Lin, G. Paniagua, Deep operator learning-based surrogate models with uncertainty quantification for optimizing internal cooling channel rib profiles, Int. J. Heat. Mass Transf. 219 (2024) 124813.

[28] Y. Yu, X.-Z. Yuan, H. Li, E. Gu, H. Wang, G. Wang, M. Pan, Current mapping of a proton exchange membrane fuel cell with a segmented current collector during the gas starvation and shutdown processes, Int. J. Hydrogen Energy 37 (2012) 15288–15300.

[29] Q. Wei, L. Fan, Z. Tu, Hydrogen production in a proton exchange membrane electrolysis cell (PEMEC) with titanium meshes as flow distributors, Int. J. Hydrogen Energy 48 (2023) 36271–36285.

[30] Y. Zhuang, P. Cui, R. Long, W. Liu, Z. Liu, Multi-objective optimization of channel structure for a proton exchange membrane water electrolysis cell, Int. J. Hydrogen Energy 49 (2024) 337–352.

[31] S. Srinivasan, Fuel Cells: From Fundamentals to Applications, Springer Science & Business media, 2006.

[32] H. Vogt, R.J. Balzer, The bubble coverage of gas-evolving electrodes in stagnant electrolytes, Electrochim. Acta 50 (2005) 2073–2079.

[33] H. Ju, H. Meng, C.-Y. Wang, A single-phase, non-isothermal model for PEM fuel cells, Int. J. Heat. Mass Transf. 48 (2005) 1303–1315.

[34] H. Meng, B. Ruan, Numerical studies of cold-start phenomena in PEM fuel cells: a review, Int. J. Energy Res. 35 (2011) 2–14.

[35] T.E. Springer, T.A. Zawodzinski, S. Gottesfeld, Polymer electrolyte fuel cell model, J. Electrochem. Soc. 138 (1991) 2334–2342.

[36] H. Ito, T. Maeda, A. Nakano, H. Takenaka, Properties of Nafion membranes under PEM water electrolysis conditions, Int. J. Hydrogen Energy 36 (2011) 10527–10540.

[37] F. Aubras, J. Deseure, J.J.A. Kadjo, I. Dedigama, J. Majasan, B. Grondin-Perez, J. P. Chabriat, D.J.L. Brett, Two-dimensional model of low-pressure PEM electrolyser: two-phase flow regime, electrochemical modelling and experimental validation, Int. J. Hydrogen Energy 42 (2017) 26203–26216.

[38] S. Toghyani, S. Fakhradini, E. Afshari, E. Baniasadi, M.Y. Abdollahzadeh Jamalabadi, M. Safdari Shadloo, Optimization of operating parameters of a polymer exchange membrane electrolyzer, Int. J. Hydrogen Energy 44 (2019) 6403–6414.

[39] H. Xiao, H. Guo, F. Ye, C. Ma, Numerical study of the dynamic response of heat and mass transfer to operation mode switching of a unitized regenerative fuel cell, Energies 9 (2016) 1015.

[40] Z. Zhan, J. Xiao, Y. Zhang, M. Pan, R. Yuan, Gas diffusion through differently structured gas diffusion layers of PEM fuel cells, Int. J. Hydrogen Energy 32 (2007) 4443–4451.

[41] S. Toghyani, E. Afshari, E. Baniasadi, Metal foams as flow distributors in comparison with serpentine and parallel flow fields in proton exchange membrane electrolyzer cells, Electrochim. Acta 290 (2018) 506–519.

[42] Q. Chen, Y. Wang, F. Yang, H. Xu, Two-dimensional multi-physics modeling of porous transport layer in polymer electrolyte membrane electrolyzer for water splitting, Int. J. Hydrogen Energy 45 (2020) 32984–32994.

[43] U. Pasaogullari, C.-Y. Wang, Two-phase transport and the role of micro-porous layer in polymer electrolyte fuel cells, Electrochim. Acta 49 (2004) 4359–4369.

[44] K. Broka, P. Ekdunge, Modelling the PEM fuel cell cathode, J. Appl. Electrochem. 27 (1997) 281–289.

[45] X.-G. Yang, Q. Ye, P. Cheng, Matching of water and temperature fields in proton exchange membrane fuel cells with non-uniform distributions, Int. J. Hydrogen Energy 36 (2011) 12524–12537.

[46] H. Park, Numerical simulations of a full-scale polymer electrolyte fuel cell with analysing systematic performance in an automotive application, Energy Convers. Manag. 103 (2015) 623–638.

[47] J. Breme, E. Eisenbarth, V. Biehl, Titanium and its alloys for medical applications. Titanium and titanium alloys, 2005.

[48] L. Xing, X. Liu, T. Alaje, R. Kumar, M. Mamlouk, K. Scott, A two-phase flow and non-isothermal agglomerate model for a proton exchange membrane (PEM) fuel cell, Energy 73 (2014) 618–634.

[49] B.E. Poling, J.M. Prausnitz, J.P. O'Connell, The Properties of Gases and Liquids, McGraw-Hill Professional, 2000.

[50] Y. Shan, S.-Y. Choe, S.-H. Choi, Unsteady 2D PEM fuel cell modeling for a stack emphasizing thermal effects, J. Power Sources 165 (2007) 196–209.

[51] J.O. Majasan, J.I.S. Cho, I. Dedigama, D. Tsaoulidis, P. Shearing, D.J.L. Brett, Two-phase flow behaviour and performance of polymer electrolyte membrane electrolysers: electrochemical and optical characterisation, Int. J. Hydrogen Energy 43 (2018) 15659–15672.

[52] S. Toghyani, E. Afshari, E. Baniasadi, S.A. Atyabi, Thermal and electrochemical analysis of different flow field patterns in a PEM electrolyzer, Electrochim. Acta 267 (2018) 234–245.